

# A light redback companion of PSR J1622–0315 and irradiation power in spider systems

Y. X. JANE YAP,<sup>1</sup> ALBERT K. H. KONG,<sup>1</sup> AND KWAN-LOK LI<sup>2</sup>

<sup>1</sup>*Institute of Astronomy, National Tsing Hua University, Hsinchu 30013, Taiwan R.O.C*

<sup>2</sup>*Department of Physics, National Cheng Kung University, Tainan 701, Taiwan R.O.C*

## ABSTRACT

We report optical observations of the millisecond pulsar binary system PSR J1622–0315 with the Lulin 1m telescope in Taiwan and the Lijiang 2.4m telescope in China between 2019 and 2021. The companion of the pulsar, which is of  $V \sim 19$  mag, showed ellipsoidal-distorted orbital variations in its light curves. The best-fit model to the light curves, with the binary code PHOEBE, gives a companion mass of  $0.122 \pm 0.006 M_{\odot}$ . This places PSR J1622–0315 in the spider-system subclass. We compared the properties of PSR J1622–0315 with other spider pulsar binaries for the scalings between the spin-down luminosity derived for the pulsar, irradiation luminosity of the companion, and X-ray luminosity of the binary. We find that pulsar irradiation in PSR J1622–0315 is insignificant and the irradiation luminosity of the transitional millisecond pulsars PSR J1023+0038 and PSR J1227–4853 are the highest among the redback systems.

*Keywords:* Compact binary stars(283); Low-mass x-ray binary stars(939); Millisecond pulsars(1062)

## 1. INTRODUCTION

Spider pulsar systems are compact binaries containing a millisecond pulsar (MSP), with a low-mass companion star, orbiting around each other in a period of  $P_b \lesssim 24$  hr. They are usually classified as black widows (BW) or redbacks (RB). The companion stars generally have masses  $\lesssim 0.1 M_{\odot}$  and  $\sim 0.1 - 0.4 M_{\odot}$  for BW and RB, respectively (see e.g. Chen et al. 2013; Roberts 2013). A rapid-spinning MSP is believed to be a phenomenon caused by the accretion of material from the companion star<sup>1</sup>. This scenario is supported by observations which showed state transition(s) between accretion-powered and rotation-powered (pulsar) state in three transitional MSPs (tMSPs): PSR J1023+0038 (Archibald et al. 2009), PSR J1227–4853 (Bassa et al. 2014) and PSR J1824–2452I (Papitto et al. 2013).

The light curve of the companion star in spider systems contains information about the irradiation of the system and the companion’s stellar properties. The effect of strong irradiation is observed in a few RBs and BWs (e.g., Breton et al. 2013; Draghis et al. 2019). Pulsar irradiation also causes evaporation of the companion star and results in the mass loss of the star (van den Heuvel & van Paradijs 1988). The evolution history of a companion star in spider systems evolving from a low-mass X-ray binary (LMXB) system under ablation was

discussed in Chen et al. (2013). The interaction between the magnetodipole radiation and a disk was proposed to explain the neutron star rotation properties in these systems, and the model was applied in transitional systems during the rotation-powered state. (Burderi et al. 2001; Papitto & Torres 2015).

In this work, we report new optical observations of PSR J1622–0315. We use Markov Chain Monte Carlo (MCMC) sampling to explore the parameter space in the models we use to fit the light curves, and to estimate the uncertainties of the masses of the components and the orbital properties of the system. We constructed a table of archival values to compare the spider systems in terms of their irradiation luminosities ( $L_{\text{irr}}$ ) inferred from the light curves, X-ray luminosities ( $L_x$ ) of the systems, and spin-down luminosities ( $\dot{E}$ ) of the pulsars.

We introduce our target and summarize our observations in Section 2. In Section 3, we describe our light curve analysis using the eclipsing binary modeling code PHOEBE (Prša et al. 2016). In Section 4, we discuss the empirical relationship between  $L_{\text{irr}}$ ,  $L_x$  and  $\dot{E}$  in BWs, RBs and tMSPs. We summarize and discuss the implications of this work in Section 5.

## 2. TARGET AND OBSERVATIONS

### 2.1. PSR J1622–0315

PSR J1622–0315 is a binary MSP discovered by Sanpa-Arsa (2016) using the Green Bank Telescope (GBT) and the Nançay telescope. It has a spin pe-

<sup>1</sup> known as the recycling scenario (Alpar et al. 1982)

**Table 1.** Observation details of MSP J1622–0315

Telescope	Date	filter (SDSS)	exposure time (s)	duration (mins)
Lulin-1m	2019 February 2	$r'$ , $g'$	180, 300	120
	2019 February 3	$r'$ , $g'$	180, 300	120
	2019 April 6	$r'$ , $g'$	180, 300	180
	2021 July 4 <sup>†</sup>	$r'$ , $g'$	180, 300	36
Lijiang- 2.4m	2019 March 10	$r'$ , $g'$	180, 300	80

<sup>†</sup> Opportunity allowed for the collection of additional quality data on July 4, 2021 with the LOT for slightly more than half an hour.

riod of 3.845 ms, and it is located at coordinates RA=16<sup>h</sup>22<sup>m</sup>59<sup>s</sup>.6 and DEC=−03°15′37.3″(J2000). The system has an orbital period of 3.9 hr and the dispersion measure is 21.4pc cm<sup>−3</sup> (~20% uncertainties; [Sanpa-Arsa 2016](#)). Radio flux variations, possibly caused by scattering with the ISM or ejected particles from the companion were also reported ([Sanpa-Arsa 2016](#)). An optical counterpart was identified with the MDM Observatory located in Arizona, United States, and its light curve exhibits an ellipsoidal variation. From the pulsar timing, the mass function was obtained and a companion mass of >0.1 M<sub>⊙</sub> was derived, assuming a neutron star (NS) mass of 1.35 M<sub>⊙</sub> and an edge-on orbit. No strong emission lines were observed in the optical spectrum of the companion of PSR J1622–0315 ([Strader et al. 2019](#)). Measurements of the companion radial velocity further allowed the neutron star mass to be constrained to >1.45 M<sub>⊙</sub> for an edge-on orbit or, alternatively, constrained the inclination to >64° if the pulsar is less massive than 2.0 M<sub>⊙</sub>. [Gentile \(2018\)](#) studied the X-ray light curve and spectrum of PSR J1622–0315 with *XMM-Newton*. Although the X-ray count rate was the lowest at the superior conjunction of the pulsar, the orbital modulation was not obvious. The X-ray spectrum was fitted with a power law of photon index  $\Gamma=2.0$  and there was no strong indication of a thermal component. Additionally, folded *Fermi*-LAT observation indicated plausible  $\gamma$ -ray pulsation ([Sanpa-Arsa 2016](#)).

## 2.2. Observations and timing analysis

We performed a series of targeted observations using the Lulin 1-m telescope (LOT) in Taiwan and the Lijiang 2.4m telescope in mainland China during the first quarter of 2019 (complemented with a shorter epoch obtained in July 2021). We used the SDSS  $r'$  and  $g'$  filters, and alternated them between each exposure. The details of the observations are listed in Table

1. The combination of our observations allowed us to cover all orbital phases, with data spanning over a few months. We only analyzed the observations which occurred when the weather conditions allowed a seeing better than FWHM  $\lesssim 3''$ . The reported light curves include 68×180 s exposures of  $r'$  images and 66×300 s exposures of  $g'$  images. Raw images were calibrated with bias and flat frames using the IRAF V2.15 standard pipelines. We performed photometry for all image frames using the IRAF package PHOT. We selected eight spherical, unsaturated point sources that are relatively isolated, as comparison stars, for all image frames. Source counts were extracted from circular apertures with 4'' radii for the target and comparison stars in the field. We extracted background counts from annular regions centered at the positions of the stars, with inner radii of 8'' and width of 2''. The photometry was performed using constant weighting, and the background rate was calculated using the centroid sky fitting algorithm. We then computed the differential photometry of PSR J1622-0315 by subtracting the average magnitudes of the comparison stars from the instrumental magnitudes of the target. The propagated errors of the measurements are shown in the error bars.

To convert the differential magnitude into apparent magnitude, we selected another stable bright star<sup>2</sup> as a reference star and calculated its differential magnitudes with the same differential photometry process described above. The differential magnitudes of the reference star varied less than 0.1 mag among the frames, which is sufficient for magnitude calibration. The apparent magnitude of the reference star is obtained from the Sloan Digital Sky Survey (SDSS) Data Release 14 catalog. The difference between the differential magnitude and the apparent magnitude of the reference star is used to calibrate the light curve of PSR J1622-0315.

The date is converted to Barycentric Julian Day (BJD) time before performing timing analysis. We performed a Lomb-scargle periodogram analysis on the selected light curves using `astropy.timeseries`. We found a period of 3.88(5) hr in the light curves (c.f. Figure 1). This period is consistent with the more precise pulsar timing solution previously reported (0.1617006798 d; [Sanpa-Arsa 2016](#)), therefore we adopted the latter in the following modeling analysis. We use  $T_0$  (ascending node of the companion) published in [Strader et al. \(2019\)](#) to fold the data. The light curve obtained is shown in Figure 2.

## 3. LIGHT CURVE MODELING

<sup>2</sup> GAIA EDR3 ID 4358429221667653632

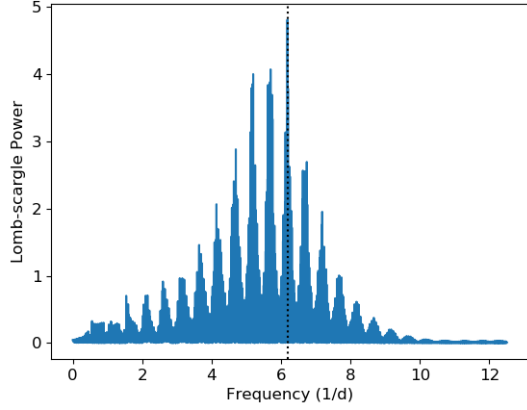


**Figure 1.** Lomb-Scargle periodogram of the combined light curves taken in 2019 for PSR J1622–0315. The peak with the strongest amplitude is located at a frequency that corresponds to a period of 0.162(2) days, indicating the orbital period of the system. Our result is consistent with the previously reported orbital period obtained using radio timing, which is indicated by a dotted line.

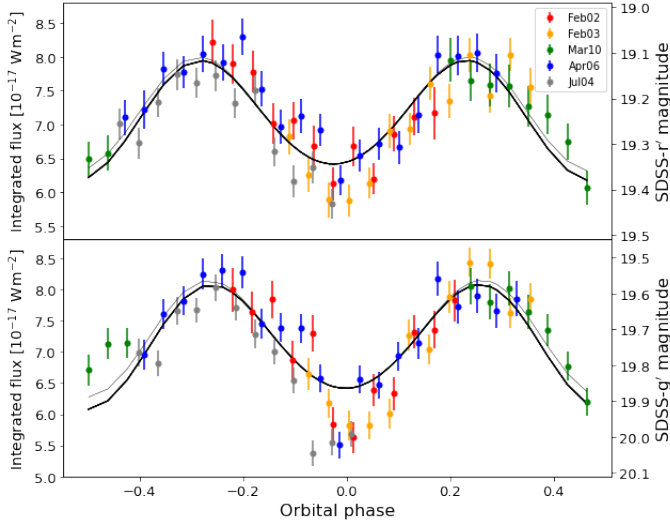


**Figure 2.** The folded light curve of PSR J1622-0315 companion in  $r'$  (top) and  $g'$  (bottom) band. Phase 0 corresponds to the inferior conjunction of the companion. The black solid line is the best-fit model from PHOEBE. The most recent dataset (2021 July 4) is not included in the fit. The gray solid line demonstrates the effect of irradiation on the companion star surface due to heating from the pulsar; the effect is most obvious at the companion superior conjunction where most of the extra irradiation is seen.

We conducted an inverse modeling analysis following the method described in Conroy et al. (2020) using PHOEBE 2.3. To begin, the apparent magnitudes are converted to the integrated fluxes using the asinh softening parameters and zero points provided in the

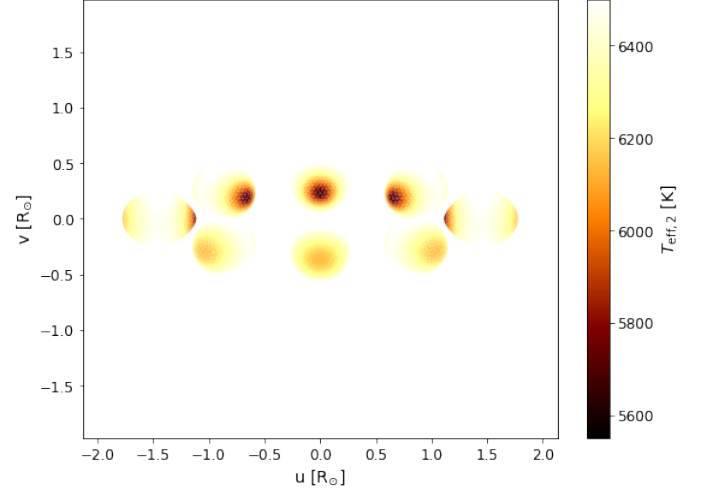


**Figure 3.** Projected view of the companion star across different orbital phases, including its effective temperature distribution. This model corresponds to the parameter values reported in Table 3.

SDSS documentation.<sup>3</sup> The  $r'$  and  $g'$  light curves are loaded into PHOEBE as separate light curve datasets with the passband set to their respective colors. We used data taken between February and April 2019, which covered the entire orbit for our analysis. The most recent dataset (2021 July 4) is not included in the modeling because it was taken substantially later compared to other datasets, to avoid possible changes in the system during this period. The position of the target with respect to the location of the telescope prevented us from achieving full orbital coverage in a single observing session of one night. While there were fluctuations between sessions, the overall ellipsoidal modulation is clearly seen in the folded light curves. We fixed the orbital period ( $P_b$ ) and the superior conjunction of the pulsar ( $T_{0,\text{sup\_conj}}$ ) using the adopted values mentioned in Sections 2.2, with an additional phase shift of 0.25 to account for the different definition of phase 0 used in PHOEBE. We also adopted the projected semi-major axis of 0.219258 lt-s from Sanpa-Arsa (2016).

We modeled PSR J1622–0315 to resemble a semi-detached binary that consists of one primary (subscript ‘1’; pulsar) and one secondary (subscript ‘2’; companion) component, where the companion star has a radius approaching the maximum allowed value before overflowing the Roche-lobe. We assumed no eclipse in the system (“*eclipse method*”=“*only horizon*”), since the light curve variation mainly comes from ellipsoidal distortion. The passband luminosity mode is set to “*abso*”

<sup>3</sup> <http://classic.sdss.org/dr6/algorithms/fluxcal.html>

*lute*” to avoid any flux rescaling. For the passband limb-darkening correction, we use a logarithmic law for the secondary star, and the coefficient is derived from the atmosphere model (Castelli & Kurucz 2004) “*ck2004*” implemented in PHOEBE. Since the optical emission from a pulsar is negligible, we can turn off the primary star contribution by setting “*distortion method*” to “*none*”. We also assumed a convective envelope for the companion star where the bolometric gravity darkening coefficient  $\beta$  is 0.08. This value is also used in the studies of similar systems (e.g. Bellm et al. 2016). The modeled system and the temperature distribution of the companion is shown in Figure 3. The inner tip of the companion star appears coldest compared to the rest of the surface; this is because the effective gravity near the tip is among the lowest under the influence of the tidal effect. The inner tip would appear brighter if significant pulsar irradiation were present.

Figure 2 also illustrates a light curve (in gray) with irradiation on the surface of the companion star caused by the pulsar. This is done by setting the irradiation method to “*wilson*” (Wilson 1990). For the primary star inputs, we changed the distortion method back to “*roche*”, and applied the effective temperature and the radius of a neutron star to allow the irradiation effect to take place. The flux of the primary star heats the surface of the secondary star, and results in an increase of temperature, especially near the inner tip of the secondary star. As shown in the light curve, the irradiation in this system is not significant (the difference in the computed loglikelihood is smaller than 0.01%); if added to the model, the effect is mostly observed at the superior conjunction of the companion star. A more severe irradiation will not reproduce the data well. Due to the uncertainty in the irradiation physics for spider MSPs, this effect is not included in the following MCMC analysis.

### 3.1. MCMC sampling

We performed a MCMC study for six system parameters: mass ratio ( $q_{\text{binary}}$ ;  $M_{\text{comp}}/M_{\text{NS}}$ ), companion’s effective temperature ( $T_{\text{eff},2}$ ), system inclination ( $i_{\text{binary}}$ ), companion radius ( $R_{\text{equiv},2}$ ), extinction parameter ( $A_V$ ) and distance ( $d$ ). We used the EMCEE (Foreman-Mackey et al. 2019) solver implemented in PHOEBE. We note that although the filling factor is more commonly used in the spider community, it is not a default parameter for detached binary models in PHOEBE. However, a volume-averaged filling factor can be derived using the critical Roche radius provided by the model.

We assigned uniform priors for  $q_{\text{binary}}$ ,  $T_{\text{eff},2}$ ,  $i_{\text{binary}}$ ,  $A_V$  and  $d$ , and a Gaussian prior for  $R_{\text{equiv},2}$ . The ranges

Lower limit	Parameter	Upper limit
0.04	$q_{\text{binary}}$	0.12
3500	$T_{\text{eff},2}$ (K)	7000
50	$i_{\text{binary}}$ ( $^\circ$ )	90
0.7	$A_V$ (mag)	0.9
1.664	$d$ (kpc)	7.766

**Table 2.** Uniform priors are used for the above fitting parameters. The prior limits are discussed in the text.

for each of the uniform priors are shown in Table 2. We chose a uniform prior for  $q_{\text{binary}}$  with limits ranging from 0.04 to 0.12 for pulsar mass ranges from  $1.4 M_\odot$  to  $2.0 M_\odot$ . Based on the binary mass function value of  $1.27 M_\odot$  (Strader et al. 2019), we set the lower limit for the system inclination at  $50^\circ$  to avoid fitting a large neutron star mass ( $>3 M_\odot$ ). For  $T_{\text{eff},2}$ , the limits are chosen based on the wide range of temperatures observed in RB companions. The  $E(B-V)$  color excess is 0.25 mag at the given coordinate and distance, by examining the Bayestar3D dust map through the python package *dustmaps* (Green et al. 2019). The color excess is then converted to  $A_V$  using  $R_V = 3.1$ . We set a uniform prior between 0.7 and 0.9 mag. Due to the degeneracy between  $A_V$ ,  $T_{\text{eff},2}$  and  $d$ , it is necessary to incorporate more than one color information in order to achieve a better fit. The distance obtained from Bailer-Jones et al. (2021) is 5843 pc with uncertainties range from 1664 pc to 7766 pc. For  $R_{\text{equiv},2}$ , we use a Gaussian prior with a mean value of  $0.27 R_\odot$ , which corresponds to roughly 90% of the critical Roche radius.

An initial sample of fitting parameters is drawn from Gaussian distributions centered around the mean of the priors. The initial sample distributions and prior distributions are chosen such that the desired parameter space can be fully explored within a reasonable computational time. We exposed the failed walkers (due to physical or backend limitations) to make sure that the parameter space is successfully covered. As demonstrated in Conroy et al. (2020), these limitations are used to constrain the parameter search space if no priors are provided explicitly.

### 3.2. MCMC results

We ran 30 walkers with 10600 iterations, where around 3000 steps were dropped as burn-in. Figure 4 shows the corner plot of the posterior distributions. We obtained a mass ratio of  $\sim 0.066$ , which is similar to that reported in Strader et al. (2019) using a radial velocity measurement. The existing degeneracy between the mass ratio



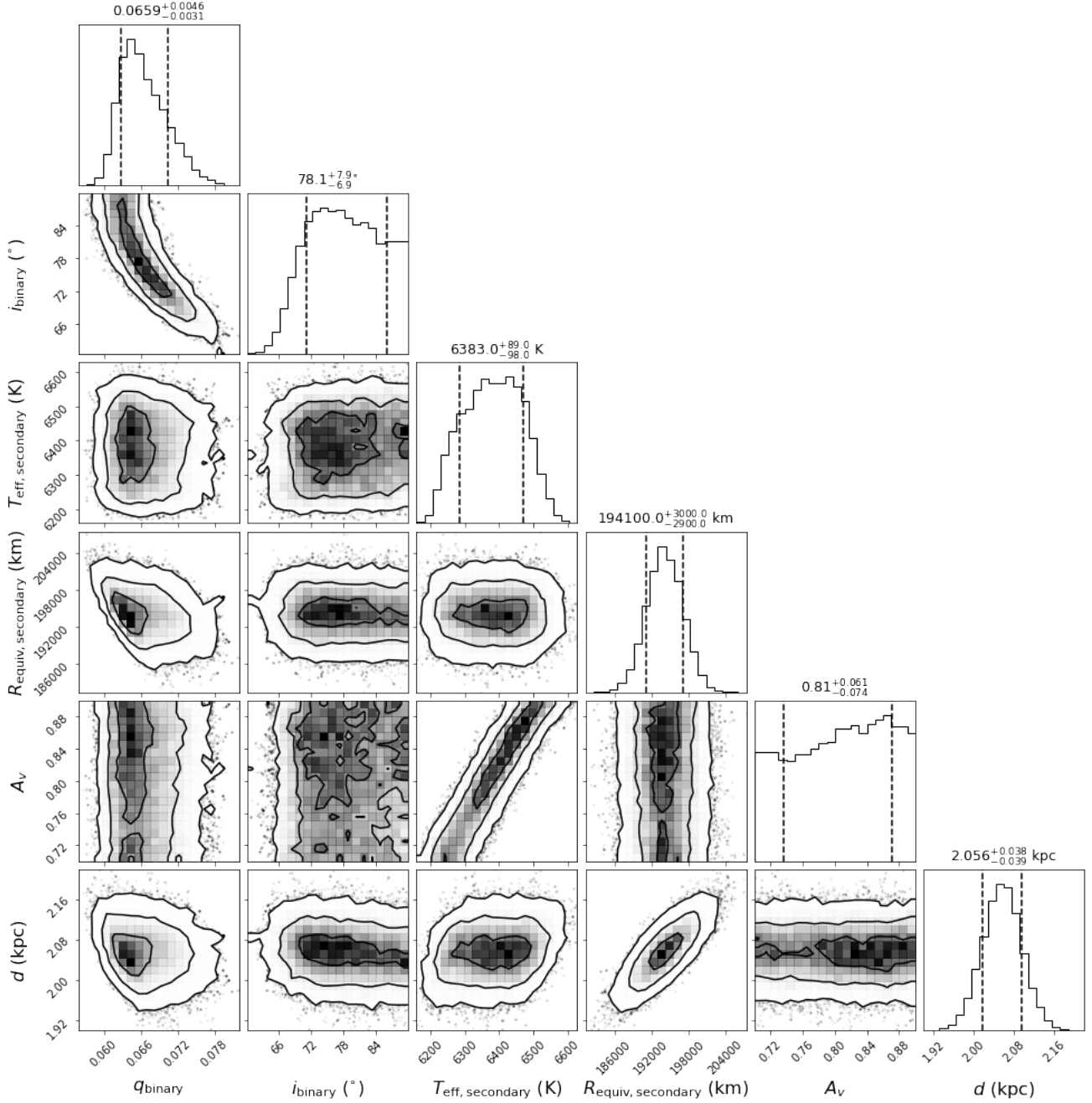


**Figure 4.** Corner plot of the posterior distributions for the fitted parameters. The median values are displayed with the respective  $1\sigma$  uncertainties, indicated by dotted lines. Degeneracy is observed in the following parameters: i)  $q_{\text{binary}}$  and  $i_{\text{binary}}$  ii)  $T_{\text{eff,secondary}}$  and  $A_V$ , iii)  $R_{\text{secondary}}$  and  $d$ . Given the data quality, we were unable to constrain the extinction parameter,  $A_V$ .

and the inclination parameter is observed. The sampled density for the companion’s effective temperature peaks around 6400 K. We note that the fitted effective temperature is higher than most known RB companions ( $\sim 3300$ – $5500$  K; see references in Table 4). The extinction parameter,  $A_V$ , is not well constrained due to the large uncertainties in our data. We obtained a system distance of  $\sim 2.1$  kpc and a companion star radius

of  $\sim 0.28 R_{\odot}$ . The determination of the distance of the system is affected by the companion star radius parameter. If the radius increases, a larger distance is required to fit the light curve. The maximum Roche radius, as a result of the orbital parameters and the mass ratio, is  $0.283 R_{\odot}$ . Hence, the volume-averaged filling factor is close to 1. A semi-detached system with a close-to-unity filling factor is common among spider systems (De Vito

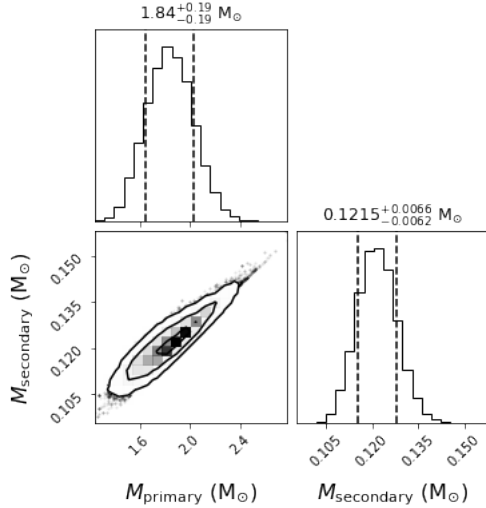


**Figure 5.** Propagated distribution of parameters  $M_{\text{primary}}$  (NS) and  $M_{\text{secondary}}$  (companion). The median values are displayed with the respective  $1\sigma$  uncertainties.

Fit parameter(s)	Result(s)
$q_{\text{binary}} [M_{\text{comp}}/M_{\text{NS}}]$	$0.066^{+0.005}_{-0.003}$
$T_{\text{eff},2}$ (K)	$6383^{+89}_{-98}$
$i_{\text{binary}}$ ( $^{\circ}$ )	$78.1^{+7.9}_{-6.9}$
$R_{\text{equiv},2}$ ( $R_{\odot}$ )	$0.279^{+0.004}_{-0.004}$
$A_V$ (mag)	$0.81^{+0.06}_{-0.07}$
$d$ (kpc)	$2.06^{+0.04}_{-0.04}$
Derived parameter(s)	
$M_{\text{primary}}$ ( $M_{\odot}$ )	$1.84^{+0.19}_{-0.19}$
$M_{\text{secondary}}$ ( $M_{\odot}$ )	$0.122^{+0.007}_{-0.006}$

**Table 3.** Best-fit results with  $1\sigma$  uncertainties.

et al. 2020). The binary masses are derived from the fitted mass ratio and inclination (c.f. Figure 5). The mass ratio implies a  $1.84\text{-}M_{\odot}$  pulsar and a  $0.122\text{-}M_{\odot}$  companion with a high inclination of  $\sim 80^{\circ}$ . All best-fit parameters are shown in Table 3. This result suggests that the PSR J1622–0315 companion is the lightest RB companion known so far.

#### 4. PULSAR IRRADIATION AND OTHER SYSTEM PROPERTIES

The interplay between the energy loss of a neutron star that gives rise to radiation and the mass transfer from the companion (which, in turn, increases the rotational energy of the pulsar) determines the evolution state of a NS low-mass X-ray binary. Many dedicated

observations have been conducted in the last decade to study the multi-wavelength properties of BWs and RBs. However, the transient nature of these systems increases the uncertainty in constraining binary evolution models. An empirical method is often used to understand the behavior of different astronomical systems. We study the relationship between the irradiation luminosity ( $L_{\text{irr}}$ ), the X-ray luminosity ( $L_x$ ), and the spin-down luminosity ( $\dot{E}$ ) in BWs, RBs and tMSPs using an empirical method. The relationship between the X-ray properties and spin-down luminosities of BWs and RBs has been previously investigated (see, e.g. Arumugasamy et al. 2015; Lee et al. 2018). In particular, using a simple power-law model, Lee et al. (2018) showed that the X-ray emission of RBs is brighter and harder compared to that of BWs. Among the spiders, tMSPs are brighter X-ray sources ( $\sim 10^{32}\text{erg s}^{-1}$  during rotation-powered state; or see Li et al. 2020).

In general, for optical modeling of BWs and RBs, the pulsar irradiation is computed as  $L_{\text{irr}} \propto (T_2^4 - T_1^4)$ , where  $T_1$  and  $T_2$  are often the base or night-side temperature and the day-side temperature of the companion. The companion is usually a low-mass star, and, depending on its spectral type, the increased temperature due to the pulsar’s irradiation on its inner face ( $\Delta T = T_2 - T_1$ ) can be more than a few thousand K for some BW systems.

We compiled a list of BWs and RBs in the Galactic field (c.f. Table 4), for which optical light curves have been previously reported. We conducted a literature review and compiled the reported irradiation luminosities. If either the spin-down energy conversion efficiency or the characteristic irradiation temperature is reported, we computed the irradiation luminosities as described in the footnotes. We dedicated a column to record the number of peaks observed in the optical light curve of each source. A tidally distorted companion without strong irradiation from the pulsar shows a two-peaked ellipsoidal light curve variation. This allows us to quickly identify the systems that are dominated by pulsar irradiation, which would otherwise show a 1-peak modulated light curve. All BWs in our sample have 1-peak modulation. We note that the detection of BW companions is more challenging since they are fainter, and we may not be able to detect them if there are less irradiated. The RBs in our sample have 1 or 2 peaks, or a combination of these two effects. The X-ray luminosity and spin-down luminosity are also included in the table; these values, where available, are based on the study of Lee et al. (2018). We also added the companion mass, spin and spin-down period to the table for complete-

Item	Designation	BW/RB <sup>(a)</sup>	$P$ (ms)	$\dot{P}$ ( $\times 10^{-21}$ ss $^{-1}$ )	Companion mass ( $M_{\odot}$ )	$L_{\text{irr}}$ ( $\times 10^{34}$ erg s $^{-1}$ )	$\log_{10}(L_x/$ erg s $^{-1}$ )	$\log_{10}(\dot{E}/$ erg s $^{-1}$ )	References
1	PSR J0023+0923	BW (1)	3.05	9.61	$0.018^{+0.002}_{-0.001}$	$0.296^{+0.016}_{-0.013}$	$29.35^{+0.47}_{-0.53}$	34.13	1,2
2	PSR J0251+2606	BW (1)	2.54	7.57	$0.032^{+0.006}_{-0.003}$	$0.252^{+0.012}_{-0.011}$	-	34.26	1,4
3	PSR J0636+5128	BW (1)	2.87	3.35	$0.018^{+0.001}_{-0.001}$	$0.097^{+0.001}_{-0.001}$	$27.93^{+1.18}_{-0.82}$	33.75	1,5
4	PSR J0952-0607	BW (1)	1.41	4.56	$0.029^{+0.001}_{-0.001}$	$2.043^{+0.077}_{-0.076}$	30.47	34.81	1,7,8,9
5	PSR J1124-3653	BW (1)	2.41	1.41	$0.041^{+0.001}_{-0.003}$	$0.286^{+0.008}_{-0.010}$	$30.56^{+0.45}_{-0.68}$	33.60	1
6	PSR J1301+0833	BW (1)	1.84	-	$0.045^{+0.001}_{-0.002}$	$0.697^{+0.046}_{-0.058}$	-	34.82	1,10
7	PSR J1311-3430	BW (1)	2.56	20.92	$0.016^{+0.001(b)}_{-0.001}$	$\sim 20$	$31.63^{+0.37}_{-0.54}$	34.69	11,12
8	PSR J1544+4937	BW (1)	2.16	2.93	$0.025^{+0.006}_{-0.006}$	$0.161^{+0.035}_{-0.035}$	-	34.06	15,16
9	PSR J1555-2908	BW (1)	1.79	44.5	$0.060^{+0.005(d)}_{-0.003}$	$9.92^{+0.002(d)}_{-0.002}$	-	35.49	3,43
10	PSR J1653.6-0158	BW (1)	1.97	2.40	$0.013^{+0.001(e)}_{-0.001}$	$0.333^{+0.039(e)}_{-0.034}$	$31.07^{+0.04}_{-0.04}$	33.64	17,18,51
11	PSR J1810+1744	BW (1)	1.66	4.60	$0.071^{+0.027(k)}_{-0.027}$	2.389	$30.68^{+0.44}_{-0.52}$	34.60	19,2
12	PSR J1959+2048	BW (1)	1.61	10.63	$0.036^{+0.001}_{-0.001}$	$3.01^{+0.036}_{-0.036}$	$31.04^{+0.32}_{-0.48}$	35.00	1,20,21
13	PSR J2017-1614	BW (1)	2.31	2.45	$_{-}^{(c)}$	-	-	33.85	22
14	PSR J2051-0827	BW (1)	4.51	12.13	$\sim 0.04$	-	$28.62^{+0.55}_{-0.70}$	33.72	23,24
15	PSR J2052+1219	BW (1)	1.99	6.70	$0.042^{+0.001}_{-0.001}$	$0.944^{+0.024}_{-0.024}$	-	34.53	1,25
16	PSR J2241-5236	BW (1)	2.19	6.65	$0.016^{+0.001}_{-0.001}$	$0.282^{+0.005}_{-0.006}$	$29.88^{+0.42}_{-0.57}$	34.40	1,26
17	PSR J2256-1024	BW (1)	2.29	12.10	$>0.030$	0.277	$30.08^{+0.37}_{-0.53}$	34.60	2
18	PSR J1023+0038	RB (1)	1.96	11.81	$0.205^{+0.008(j,f)}_{-0.008}$	0.884	$31.90^{+0.31(i)}_{-0.75}$	34.40	27,29,2
19	PSR J1048+2339	RB (1)	4.67	30.37	$0.24-0.35$	$0.759^{+0.210}_{-0.175}$	$31.52^{+0.18(h)}_{-0.18}$	34.08	30,31,32
20	PSR J1227-4853	RB (1)	1.69	11.11	$0.17^{+0.01(j,f)}_{-0.01}$	$\sim 1.21^{(f)}$	$32.12^{+0.31(i)}_{-0.47}$	34.96	27,33,34
21	PSR J1306-40	RB (1)	2.20	-	$0.59^{+0.01(g)}_{-0.01}$	$\sim 5.90^{(g)}$	31.94	-	35,36,47
22	PSR J1431-4715	RB (2)	2.01	14.11	0.13 - 0.19	-	-	34.83	37,38
23	PSR J1622-0315	RB (2)	3.85	11.6	$0.122^{+0.007}_{-0.006}$	-	$30.61^{+0.07(h)}_{-0.07}$	33.89	39,40,41
24	PSR J1628-3205	RB (2)	3.21	15.06	0.17 - 0.24	-	$30.96^{+0.33}_{-0.50}$	34.26	10
25	PSR J1723-2837	RB (2)	1.86	7.56	$0.36^{+0.08}_{-0.06}$	-	$31.92^{+0.31}_{-0.48}$	34.67	42,44,38
26	PSR J2039-5617	RB (2)	2.65	14.16	0.162 - 0.18	$0.150^{+0.027}_{-0.018}$	$31.18^{+0.03(h)}_{-0.03}$	34.40	38,28,13,49
27	PSR J2129-0429	RB (2)	7.62	335.6	$0.44^{+0.04}_{-0.04}$	$0.091^{+0.018}_{-0.018}$	$31.79^{+0.34}_{-0.51}$	34.48	45,46
28	PSR J2215+5135	RB (1)	2.61	33.37	$0.345^{+0.008(k)}_{-0.007}$	0.794	$31.92^{+0.41}_{-0.61}$	34.87	19,2
29	PSR J2339-0533	RB (1)	2.88	6.68	$0.30^{+0.02(l)}_{-0.02}$	$0.316^{+0.073}_{-0.073}$	$31.44^{+0.33}_{-0.49}$	34.04	48,50

**References.** (1) Draghis et al. (2019), (2) Breton et al. (2013), (3) Kennedy et al. (2022), (4) Deneva et al. (2021), (5) Stovall et al. (2014), (6) Spiewak et al. (2016), (7) (0.3-10 keV) Ho et al. (2019), (8), Bassa et al. (2017), (9) Nieder et al. (2019), (10) Li et al. (2014), (11) Romani et al. (2012), (12) Ray et al. (2013), (13) Clark et al. (2021), (14) (2-10keV) Lee et al. (2018), (15) Tang et al. (2014), (16) Bhattacharyya et al. (2013), (17) Kong et al. (2014), (18) Nieder et al. (2020), (19) Schroeder & Halpern (2014), (20) Guillemot et al. (2012), (21) Huang et al. (2012), (22) Sanpa-Arsa (2016), (23) Stappers et al. (2001), (24) Espinoza et al. (2013), (25) Zharikov et al. (2019), (26) Keith et al. (2011), (27) Stringer et al. (2021), (28) (0.5-8 keV) Bogdanov et al. (2021), (29) Bogdanov et al. (2011), (30) Deneva et al. (2016), (31) (0.3-10 keV) Miraval Zanon et al. (2021), (32) Yap et al. (2019), (33) Roy et al. (2015), (34) Bogdanov et al. (2014), (35) Swihart et al. (2019), (36) (0.5-10 keV) Linares (2018), (37) Bates et al. (2015), (38) Strader et al. (2019), (39) this work, (40) Sanpa-Arsa (2016), (41) (0.2-10 keV) Gentile (2018), (42) Crawford et al. (2013), (43) Ray et al. (2022), (44) van Staden & Antoniadis (2016), (45) Bellm et al. (2016), (46) Hui et al. (2015), (47) Keane et al. (2018), (48) Kandel et al. (2020), (49) Romani (2015), (50) Romani & Shaw (2011), (51) Long et al. (2022).

**Notes.**

$-\dot{P}, \tau, L_x, \dot{E}$  are taken from reference (14) and the references therein, unless otherwise stated.  
 -Irradiation power is calculated using  $L_{\text{irr}} = 4\pi a^2 \sigma (T_2^4 - T_1^4)$  or  $L_{\text{irr}} = \epsilon \dot{E}$ , depending on the available information.  
 Items: <sup>(a)</sup> Number of optical peak(s). <sup>(b)</sup> Parameters from the ‘Eq Hot Spots’ model are used. <sup>(c)</sup> No light curve derived parameters. <sup>(d)</sup>  $1\sigma$  value is used. <sup>(e)</sup> Parameters from the ‘Veiled model’ are used. <sup>(f)</sup> Parameters from the ‘HR2’ model are used;  $a = 0.97R_{\odot}$  obtained from reference (33). <sup>(g)</sup> Temperatures from the ‘No spot’ model are used;  $a$  is calculated using  $T = 2\pi\sqrt{a^3/G/(M_1 + M_2)}$ . <sup>(h)</sup>  $\Delta(\log L_x) = (\Delta L/L)/\ln 10$ . <sup>(i)</sup> Rotation-powered state. <sup>(j)</sup> Companion mass is calculated using the reported pulsar mass and binary mass ratio. <sup>(k)</sup> Parameters from the ‘NextGen’ model are used. <sup>(l)</sup> Parameters from the ‘HS’ model are used.

**Table 4.** A compilation of spider MSPs with published optical counterparts.

ness. The tMSP parameters in the table correspond to the radio pulsar state.

As mentioned in the Introduction, spiders systems are believed to have evolved from LMXB systems. Therefore, it is useful to compare the X-ray properties of these systems to the irradiation luminosity experienced by the companions. Such a comparison allows us to evaluate the total energy available, and the evolution of the luminosity in these systems that suffer constant ablation (Levinson & Eichler 1991). The left panel of Figure 6 shows the relationship between irradiation luminosity and X-ray luminosity. The irradiation luminosity is of about 2 orders of magnitude higher than the X-ray luminosity, and therefore the X-ray emission, regardless of its origin, is unlikely to be the main source of irradiation in these systems. A RB system with higher X-ray luminosity could be experiencing weak accretion activity at some stages; on the other hand, BW systems are dominated by the pulsar irradiation, hence they are not accreting systems. We performed a linear regression analysis for the two variables using the `scipy` package `linregress`. The Pearson correlation coefficients are 0.56 and 0.75, for RBs and BWs respectively. The two variables are related by  $\log_{10} L_{\text{irr}} = 0.74 \log_{10} L_{\text{x}} + 10.11$  for RBs, and  $\log_{10} L_{\text{irr}} = 0.50 \log_{10} L_{\text{x}} + 18.60$  for BWs. In our samples, all four highly irradiated BWs (ID: 4, 7, 11, 12) have high X-ray and spin-down luminosity compared to other BWs. The irradiation luminosity gap observed in the  $L_{\text{irr}}-L_{\text{x}}$  plot for BWs (i.e.  $0.3 \times 10^{34} \text{ erg s}^{-1} \lesssim L_{\text{irr,BW}} \lesssim 2 \times 10^{34} \text{ erg s}^{-1}$ ) corresponds to characteristic irradiation temperatures of  $5400 \text{ K} \lesssim T_{\text{irr}} \lesssim 8700 \text{ K}$ , assuming an orbital separation of one solar radius. By applying the empirical relation we obtained for BW systems and substituting for the rough upper and lower bounds of the observed gap, we found that the resulting X-ray luminosity is  $L_{\text{x}} \in (6 \times 10^{29}, 2 \times 10^{31}) \text{ erg s}^{-1}$ . In the plot, we show that the X-ray counterpart of some of the BWs falls within this range, suggesting that the irradiation luminosity gap is likely not an observational bias. We note that the derived irradiation temperature is dependent on the model used, and is subject to the variable nature of spiders (e.g. the pulsar heating in PSR J1048+2339 became significant in less than two weeks; Yap et al. 2019), however this should not affect the general trend reported. The tMSPs are the brightest among the RBs in both irradiation and X-ray luminosity.

The right panel of Figure 6 shows the relationship between irradiation luminosity and spin-down luminosity. The order of magnitudes between the two luminosities are similar ( $\sim 10^{33} - 10^{35} \text{ erg s}^{-1}$ ). For PSR J1622-0315, while the system is dominated by ellipsoidal distortion,

we cannot rule out the presence of pulsar irradiation. Therefore, we present the irradiation luminosity of PSR J1622-0315 as an upper limit in the same figure, where the effective temperature is used as the characteristic irradiation temperature. The error bar corresponds to  $1\sigma$  uncertainty from the fitting results. Given that a system requires more energy to raise the temperature of a hotter star compared to a cooler star, and the effective temperature in PSR J1622-0315 is relatively higher among other spider companions, an irradiation temperature of  $T_{\text{irr}} \approx T_{\text{eff}} = 6400 \text{ K}$  corresponds to a day-side temperature  $T_2 = 7300 \text{ K}$  (if  $T_1 = 6000 \text{ K}$ ). A considerable amount of energy is required to achieve this temperature difference, hence the effective temperature is used as an approximation to estimate the upper limit of pulsar irradiation in PSR J1622-0315.

In analogy to the conversion efficiency from spin-down power to X-ray luminosity (Fig. 10 in Arumugasamy et al. 2015) and  $\gamma$ -ray luminosity (Fig. 11 in Strader et al. 2019), we added analytic lines that correspond to  $L_{\text{irr}}/\dot{E}$  for comparison. A conversion efficiency would suggest that the heating mechanism involves some form of reprocessing of the spin-down energy. A theoretical study of this would be useful, but beyond the scope of this paper. The  $L_{\text{irr}}-\dot{E}$  relationship for BWs and RBs are similar in that they scatter across the parameter space despite the companion stars having masses well separated into two groups. However, one of the BWs, PSR J1311-3430 has an irradiation luminosity that exceeds its spin-down luminosity ( $L_{\text{irr}} > \dot{E}$ ; conversion efficiency greater than 100%), in contrast to other systems that have  $L_{\text{irr}} < \dot{E}$ . It is likely that a less irradiated BW system would have a low conversion efficiency of only a few percent, and would be faint and challenging to observe. To complement the  $L_{\text{irr}}-\dot{E}$  plot, in Figure 7 we show the  $P-\dot{P}$  diagram of the pulsars in known spider systems. The spin periods ( $P$ ) of the pulsar in RBs and BWs are similar, but the pulsars in a RB system occupy the space with higher  $\dot{P}$  values compared to the pulsars in a BW system. We note that the tMSPs (marked red stars) have very similar  $P$  and  $\dot{P}$  values. We added the MSP spin-up line, reproduced from a recent study reported by Liu et al. (2022). This information is useful for comparing the spin profile of irradiated transitional systems, which is outside the scope of this paper.

## 5. SUMMARY

PSR J1622-0315 was discovered in the pulsar search of *Fermi* unassociated sources using the GBT and the optical counterpart was identified (Sanpa-Arsa 2016). The light curve showed a clear orbital variation and fluctuations at the same orbital phase. Strader et al.



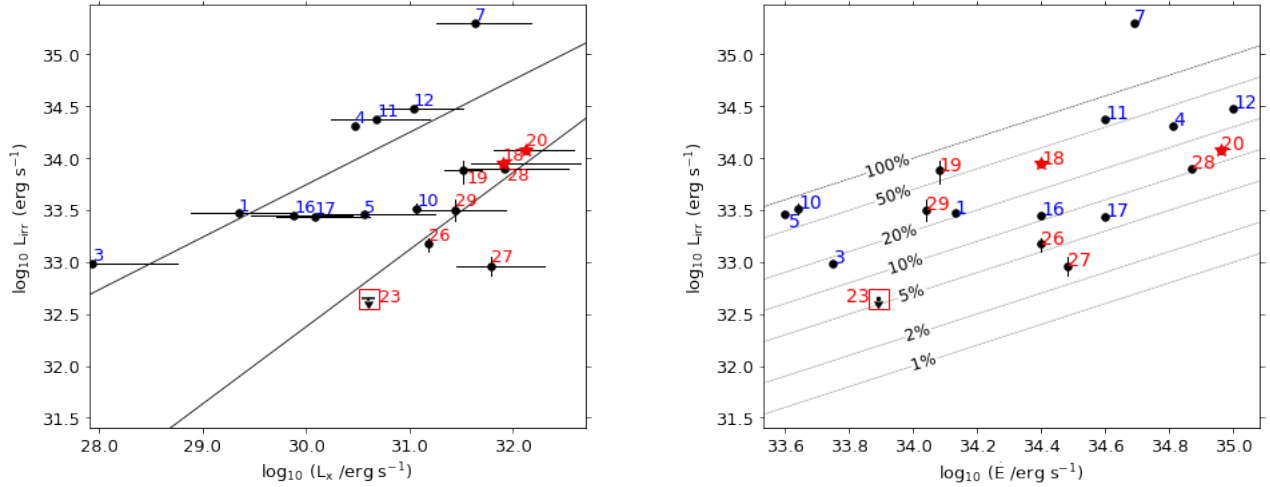


**Figure 6.** (Left) A comparison between the irradiation luminosity and the X-ray luminosity. (Right) A comparison between the irradiation luminosity and the spin-down luminosity. The ID of BWs are labelled in blue while RBs are labelled in red. tMSPs (ID: 18, 20) are marked as red stars. The upper limit of irradiation luminosity of PSR J1622-0315 (marked by a red square box) is calculated using the effective temperature. The RBs and BWs occupy two distinct regions in the  $L_{\text{irr}}-L_x$  plot. The dotted lines in  $L_{\text{irr}}-\dot{E}$  plot correspond to different  $L_{\text{irr}}/\dot{E}$  ratios. PSR J1311-3430 (ID: 7) is the only source in our study that has  $L_{\text{irr}} > \dot{E}$ .

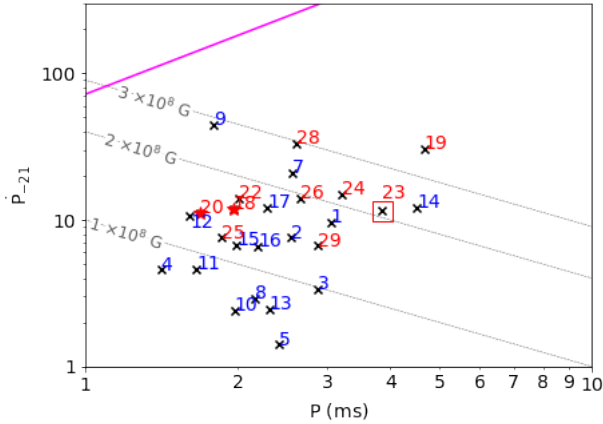


**Figure 7.** A complimentary  $P-\dot{P}$  diagram of the pulsars in spider systems shown in logarithmic scale where  $\dot{P}_{-21} = \dot{P}/10^{-21}$ . The characteristic magnetic field strengths are indicated by dashed gray lines. The ID of BWs are labelled in blue while RBs are labelled in red. tMSPs are marked as red stars. The magenta line shows the MSP spin-up line according to Liu et al. (2022).

(2019) published the radial velocity and spectra of PSR J1622-0315, and the companion mass was constrained to  $0.10-0.14 M_{\odot}$ .

In this work, we modeled the light curve of PSR J1622-0315 using the PHOEBE code. We performed MCMC sampling on six system parameters and found that the pulsar irradiation on the companion is not significant in this system (c.f. Fig. 2). The result obtained constrained the pulsar mass to  $1.84^{+0.19}_{-0.19} M_{\odot}$  and the companion mass to  $0.122^{+0.007}_{-0.006} M_{\odot}$ . From the MCMC

result, we find that PSR J1622-0315 is the lightest known redback system with a relatively hot companion. We note that PSR J1622-0315 has an orbital period of 0.16 d, which is slightly smaller than other RBs ( $\gtrsim 0.2$  d).

Additionally, we studied the energetic relationship between irradiation luminosity ( $L_{\text{irr}}$ ), X-ray luminosity ( $L_x$ ) and the pulsar's spin-down luminosity ( $\dot{E}$ ) of spider systems. Both BWs and RBs show a correlation in their  $L_{\text{irr}}$  and  $L_x$  values, with BWs having a higher Pearson correlation of 0.75. We find that PSR J1622-0315 lies well within the RB group with insignificant pulsar irradiation. PSR J1622-0315 also has the smallest X-ray and spin-down luminosity among the RBs in the sample. Observations of borderline-mass (companion) spiders like PSR J1622-0315 and PSR J1810+1744 (Schroeder & Halpern 2014) are important to constrain the binary evolution model. Recent findings suggest that both NS low-mass X-ray binaries and spider systems tend to have an ionized and clumpy environment (Knight et al. 2023), implying that pulsar irradiation and mass loss in the form of winds are common in different evolution stages. Assuming the presence of pulsar irradiation, it is useful to compare the companion star behavior to the neutron star properties as they co-evolve with each other. For instance, in this study, both tMSPs are the RB systems with the highest pulsar irradiation luminosity and X-ray luminosity compared to other spider systems, and this suggests that the transitional systems are in general more energetic. Provided the system is bright enough to be observed, both light curve

modeling of the irradiation properties and spectral observation can be used together to study the evolution of the companion under pulsar irradiation. Finally, the estimation of irradiation luminosity is model-dependent and is subject to the variable nature of these systems, which may not be fully reflected in this study.

We thank the referee for his/her many useful scientific suggestions and comments. This work has made use of data collected at Lulin Observatory, partly supported by the National Science and Technology Council of the Republic of China (Taiwan) through grant 105-2112-M-008-024-MY3. Y.X.J.Y and A.K.H.K. are supported by the National Science and Technology Council of the Re-

public of China (Taiwan) through grants 110-2628-M-007-005 and 111-2112-M-007-020. KLL is supported by the Ministry of Science and Technology of the Republic of China (Taiwan) through grant 110-2636-M-006-013, and he is a Yushan (Young) Scholar of the Ministry of Education of the Republic of China (Taiwan). This work used high-performance computing facilities operated by the Center for Informatics and Computation in Astronomy (CICA) at National Tsing Hua University. This equipment was funded by the Ministry of Education of Taiwan, the Ministry of Science and Technology of Taiwan, and National Tsing Hua University. We thank Kinwah Wu and Kaye Li for their advice to improve the readability of the manuscript.

## REFERENCES

- Alpar, M. A., Cheng, A. F., Ruderman, M. A., & Shaham, J. 1982, *Nature*, 300, 728
- Archibald, A. M., Stairs, I. H., Ransom, S. M., et al. 2009, *Science*, 324, 1411
- Arumugasamy, P., Pavlov, G. G., & Garmire, G. P. 2015, *ApJ*, 814, 90
- Bailer-Jones, C. A. L., Rybizki, J., Fouesneau, M., Demleitner, M., & Andrae, R. 2021, *AJ*, 161, 147
- Bassa, C. G., Patruno, A., Hessels, J. W. T., et al. 2014, *MNRAS*, 441, 1825
- Bassa, C. G., Pleunis, Z., Hessels, J. W. T., et al. 2017, *ApJL*, 846, L20
- Bates, S. D., Thornton, D., Bailes, M., et al. 2015, *MNRAS*, 446, 4019
- Bellm, E. C., Kaplan, D. L., Breton, R. P., et al. 2016, *ApJ*, 816, 74
- Bhattacharyya, B., Roy, J., Ray, P. S., et al. 2013, *ApJL*, 773, L12
- Bogdanov, S., Archibald, A. M., Hessels, J. W. T., et al. 2011, *ApJ*, 742, 97
- Bogdanov, S., Bahramian, A., Heinke, C. O., et al. 2021, *ApJ*, 912, 124
- Bogdanov, S., Patruno, A., Archibald, A. M., et al. 2014, *ApJ*, 789, 40
- Breton, R. P., van Kerkwijk, M. H., Roberts, M. S. E., et al. 2013, *ApJ*, 769, 108
- Burderi, L., Possenti, A., D’Antona, F., et al. 2001, *ApJL*, 560, L71
- Castelli, F., & Kurucz, R. L. 2004, *A&A*, 419, 725
- Chen, H.-L., Chen, X., Tauris, T. M., & Han, Z. 2013, *ApJ*, 775, 27
- Clark, C. J., Nieder, L., Voisin, G., et al. 2021, *MNRAS*, 502, 915
- Conroy, K. E., Kochoska, A., Hey, D., et al. 2020, *ApJS*, 250, 34
- Crawford, F., Lyne, A. G., Stairs, I. H., et al. 2013, *ApJ*, 776, 20
- De Vito, M. A., Benvenuto, O. G., & Horvath, J. E. 2020, *MNRAS*, 493, 2171
- Deneva, J. S., Ray, P. S., Camilo, F., et al. 2016, *ApJ*, 823, 105
- . 2021, *ApJ*, 909, 6
- Draghis, P., Romani, R. W., Filippenko, A. V., et al. 2019, *ApJ*, 883, 108
- Espinoza, C. M., Guillemot, L., Çelik, Ö., et al. 2013, *MNRAS*, 430, 571
- Foreman-Mackey, D., Farr, W., Sinha, M., et al. 2019, *The Journal of Open Source Software*, 4, 1864
- Gentile, P. A. 2018, PhD thesis, West Virginia University
- Green, G. M., Schlafly, E., Zucker, C., Speagle, J. S., & Finkbeiner, D. 2019, *ApJ*, 887, 93
- Guillemot, L., Johnson, T. J., Venter, C., et al. 2012, *ApJ*, 744, 33
- Ho, W. C. G., Heinke, C. O., & Chugunov, A. I. 2019, *ApJ*, 882, 128
- Huang, R. H. H., Kong, A. K. H., Takata, J., et al. 2012, *ApJ*, 760, 92
- Hui, C. Y., Hu, C. P., Park, S. M., et al. 2015, *ApJL*, 801, L27
- Kandel, D., Romani, R. W., Filippenko, A. V., Brink, T. G., & Zheng, W. 2020, *ApJ*, 903, 39
- Keane, E. F., Barr, E. D., Jameson, A., et al. 2018, *MNRAS*, 473, 116
- Keith, M. J., Johnston, S., Ray, P. S., et al. 2011, *MNRAS*, 414, 1292

- Kennedy, M. R., Breton, R. P., Clark, C. J., et al. 2022, *MNRAS*, 512, 3001
- Knight, A. H., Ingram, A., van den Eijnden, J., et al. 2023, *MNRAS*, 520, 3416
- Kong, A. K. H., Jin, R., Yen, T. C., et al. 2014, *ApJL*, 794, L22
- Lee, J., Hui, C. Y., Takata, J., et al. 2018, *ApJ*, 864, 23
- Levinson, A., & Eichler, D. 1991, *ApJ*, 379, 359
- Li, K.-L., Strader, J., Miller-Jones, J. C. A., Heinke, C. O., & Chomiuk, L. 2020, *ApJ*, 895, 89
- Li, M., Halpern, J. P., & Thorstensen, J. R. 2014, *ApJ*, 795, 115
- Linares, M. 2018, *MNRAS*, 473, L50
- Liu, X.-J., You, Z.-Q., & Zhu, X.-J. 2022, *ApJL*, 934, L2
- Long, J. S., Kong, A. K. H., Wu, K., et al. 2022, *ApJ*, 934, 17
- Miraval Zanon, A., D’Avanzo, P., Ridolfi, A., et al. 2021, *A&A*, 649, A120
- Nieder, L., Clark, C. J., Bassa, C. G., et al. 2019, *ApJ*, 883, 42
- Nieder, L., Clark, C. J., Kandel, D., et al. 2020, *ApJL*, 902, L46
- Papitto, A., & Torres, D. F. 2015, *ApJ*, 807, 33
- Papitto, A., Ferrigno, C., Bozzo, E., et al. 2013, *Nature*, 501, 517
- Prša, A., Conroy, K. E., Horvat, M., et al. 2016, *ApJS*, 227, 29
- Ray, P. S., Ransom, S. M., Cheung, C. C., et al. 2013, *ApJL*, 763, L13
- Ray, P. S., Nieder, L., Clark, C. J., et al. 2022, *ApJ*, 927, 216
- Roberts, M. S. E. 2013, in *Neutron Stars and Pulsars: Challenges and Opportunities after 80 years*, ed. J. van Leeuwen, Vol. 291, 127–132
- Romani, R. W. 2015, *ApJL*, 812, L24
- Romani, R. W., Filippenko, A. V., Silverman, J. M., et al. 2012, *ApJL*, 760, L36
- Romani, R. W., & Shaw, M. S. 2011, *ApJL*, 743, L26
- Roy, J., Ray, P. S., Bhattacharyya, B., et al. 2015, *ApJL*, 800, L12
- Sanpa-Arsa, S. 2016, PhD thesis, University of Virginia
- Schroeder, J., & Halpern, J. 2014, *ApJ*, 793, 78
- Spiewak, R., Kaplan, D. L., Archibald, A., et al. 2016, *ApJ*, 822, 37
- Stappers, B. W., van Kerkwijk, M. H., Bell, J. F., & Kulkarni, S. R. 2001, *ApJL*, 548, L183
- Stovall, K., Lynch, R. S., Ransom, S. M., et al. 2014, *ApJ*, 791, 67
- Strader, J., Swihart, S., Chomiuk, L., et al. 2019, *ApJ*, 872, 42
- Stringer, J. G., Breton, R. P., Clark, C. J., et al. 2021, *MNRAS*, 507, 2174
- Swihart, S. J., Strader, J., Chomiuk, L., & Shishkovsky, L. 2019, *ApJ*, 876, 8
- Tang, S., Kaplan, D. L., Phinney, E. S., et al. 2014, *ApJL*, 791, L5
- van den Heuvel, E. P. J., & van Paradijs, J. 1988, *Nature*, 334, 227
- van Staden, A. D., & Antoniadis, J. 2016, *ApJL*, 833, L12
- Wilson, R. E. 1990, *ApJ*, 356, 613
- Yap, Y. X., Li, K. L., Kong, A. K. H., et al. 2019, *A&A*, 621, L9
- Zharikov, S., Kirichenko, A., Zyuzin, D., Shibano, Y., & Deneva, J. S. 2019, *MNRAS*, 489, 5547